Interplay between Structural and Thermoelectric Properties in Epitaxial $Sb_{2+x}Te_3$ Alloys

Stefano Cecchi*, Daniele Dragoni, Dominik Kriegner, Elisa Tisbi, Eugenio Zallo, Fabrizio Arciprete, Václav Holý, Marco Bernasconi, Raffaella Calarco

Dr. S. Cecchi, Dr. E. Zallo, Prof. F. Arciprete, Dr. R. Calarco
Paul-Drude-Institut für Festkörperelektronik, Hausvogteiplatz 5-7, D-10117 Berlin, Germany
E-mail: cecchi@pdi-berlin.de
Dr. D. Dragoni, Prof. M. Bernasconi
Department of Materials Science, University of Milano-Bicocca, via R. Cozzi 55, 20125 Milano, Italy
Dr. D. Kriegner, Prof. V. Holy
Department of Condensed Matter Physics, Faculty of Mathematics and Physics, Charles University, Ke Karlovu 5,12116 Praha, Czech Republic
Dr. D. Kriegner
Max-Planck-Institute for Chemical Physics of Solids, Nöthnitzer Straße 40, 01187 Dresden, Germany
E. Tisbi, Prof. F. Arciprete
Dipartimento di Fisica, Università di Roma "Tor Vergata", Via della Ricerca Scientifica 1, I-00133 Rome, Italy
Prof. V. Holy
CEITEC at Masaryk University, Kotlářská 2, 611 37 Brno, Czech Republic

In recent years strain engineering has been proposed in chalcogenide superlattices to shape in particular the switching functionality for phase change memory applications. This is possible in Sb_2Te_3/GeTe heterostructures leveraging on the peculiar behavior of Sb_2Te_3, in between covalently bonded and weakly bonded materials. In the present study the structural and thermoelectric properties of epitaxial $Sb_{2+x}Te_3$ films are shown, as they represent an intriguing option to expand the horizon of strain engineering in such superlattices. Samples with composition between Sb_2Te_3 and Sb_4Te_3 have been prepared by molecular beam epitaxy. A combination of X-ray diffraction and Raman spectroscopy, together with dedicated simulations, allows unveiling the structural characteristics of the alloys. A consistent evaluation of the structural disorder characterizing the material is drawn, as well as the presence of both Sb_2 and Sb_4 slabs is detected. A strong link exists among structural and

thermoelectric properties, the latter having implications also in phase change superlattices. A further improvement of the thermoelectric performances may be achieved by accurately engineering the intrinsic disorder. The possibility to tune the strain in designed $Sb_{2+x}Te_3$/GeTe superlattices by controlling at the nanoscale the two dimensional character of the $Sb_{2+x}Te_3$ alloys is envisioned.

1. Introduction

Since the discovery of graphene, [1,2] two dimensional (2D) materials and related van der Waals (vdW) heterostructures have quickly become a vast playground for both basic and applied materials research, promising disruptive implications in flexible and transparent electronics as well as optoelectronics. [3] With respect to heterostructures prepared by exfoliation technique, [4] vdW epitaxy [5] guarantees better purity and scalability, both pivotal for device processing and implementation with the well established Si technology. Antimony telluride (Sb_2Te_3) is a layered chalcogenide material formed by quintuple layers (QLs) bonded to each other by vdW forces. It has been studied for its topological insulating surface states [6] and used as building block in phase change memory (PCM) and thermoelectric (TE) superlattice (SL) structures. [7,8] A small interaction between substrate and epilayer has been shown for Sb_2Te_3 grown by molecular beam epitaxy (MBE) on both Si(111) [9] and graphene. [10] Very recently our group demonstrated an intriguing deviation from such a purely 2D material behavior. [11,12] Indeed, in epitaxial Sb_2Te_3/GeTe SLs a partial coupling develops between the constituting Sb_2Te_3 and GeTe layers. Strikingly, an unparalleled tunable distribution of lattice parameters develops in the heterostructures allowing also to realize strain engineering in such weakly coupled systems. This is of high interest, since strain engineering in chalcogenide SLs has been proposed for improved switching performance. [13,14] Similarly, the influence of strain on the TE transport in Bi_2Te_3 and Sb_2Te_3 has been investigated following a classical approach. [15]

Here we investigate $Sb_{2+x}Te_3$ alloys grown epitaxially by MBE on silicon substrate. Several antimony telluride lamellar phases exist in the homologous series $(Sb_2Te_3)_m(Sb_2)_n$, in which Sb_2 double layers (DLs) are inserted between Sb_2Te_3 QLs forming ordered stacking sequences (also named adaptive natural SLs). [16,17] While the composition related increase of the lattice parameter is well known and used in Ref. [14], the tuning of the 2D character of $Sb_{2+x}Te_3$ by finely controlling the excess of Sb in the material (i.e. to strengthen the coupling) may provide an additional tool to tailor the functionality of chalcogenide SLs. Moreover, the evolution of TI properties as a function of composition has been reported in layered chalcogenides. [18–20] Since for compositions between Sb_2Te_3 and Sb_4Te_3 the vdW gaps are progressively filled by the Sb DLs, the range of interest of our study is $Sb_{2+x}Te_3$ alloys with x between 0 and 2. In addition, considering PCM devices we remind that even small deviations of the GeSbTe (GST) composition affect markedly both electrical and thermal parameters. [21] Furthermore, as shown for the electrical transport properties of Sb_2Te_3/GeTe SLs, [22] the understanding and control of disorder which could be achieved by MBE may allow tailoring the thermoelectric properties of $Sb_{2+x}Te_3$ alloys.

In the following we focus exemplary on Sb_4Te_3. The crystal structure of Sb_4Te_3 is as well lamellar, however, two possible stacking orders are proposed in literature. Poudeu and Kanatzidis [17] reported a "two to two" (2/2) stacking of two Sb DLs (Sb_4) alternated with two Sb_2Te_3 QLs belonging to the *R-3m* space group (**Figure 1**(a)). Instead Kifune et al. [23] suggested a "one to one" (1/1) stacking of a single Sb DL (Sb_2) followed by a QL (Figure 1(b)). However, the structure was not directly observed. The continuous evolution from Sb_2Te_3 to $Sb_{72}Te_{28}$ *R-3m* space group crystals motivated the claim. Remarkably, the bonding nature of the Sb_4Te_3 1/1 and 2/2 sequences is different, since only in the latter case a vdW gap is present between adjacent QLs. [17] Thus discerning and potentially controlling between the two structures is paramount to allow for strain engineering in such weakly coupled systems.

2. Growth and X-Ray Diffraction

Details about the growth of epitaxial $Sb_{2+x}Te_3$ films are reported in Section 6. Starting from stoichiometric Sb_2Te_3, [9] the composition of $Sb_{2+x}Te_3$ was controlled by increasing the Sb/Te atomic flux ratio, providing the Sb excess by decreasing the Te at fixed Sb flux. In **Figure 2**(a) the radial scans of the $Sb_{2+x}Te_3$ samples on normal Si(111) are shown (dotted lines). The sharp peaks at ~ 2, 4 and 6 $Å^{-1}$ correspond to the (111), (222), and (333) Bragg reflections of the Si substrate. The Sb_2Te_3 radial scan (brown curve) is characterized by a series of Bragg reflections along the symmetric rod (00.3l), reflecting its highly periodic layered structure. The separation between the peaks allows inferring the c lattice constant (30.44 ± 0.11 Å), which is very close to previous reports. [24,25] In analogy to the $Bi_{2+x}Te_3$ system, [26] the excess of Sb produces remarkable structural changes in the material, as testified by the continuous evolution of the diffraction curves. Besides a reduction of the Q_z separation between 00.[3*(2+3l)] and 00.[3*(3+3l)] Sb_2Te_3 peaks (00.6-00.9, 00.15-00.18, 00.24-00.27 in Figure 2(a)), which is attributed to the overall increase of the c lattice parameter from Sb_2Te_3 to Sb_4Te_3 (and beyond), it is worth to emphasize the following points. i) Double peak features appear when low excess of Sb is provided (orange curve). Sb_2Te_3 00.12 and 00.21 peaks split, while shoulders at lower Q_z values are visible for 00.6 and 00.15 peaks. ii) The separation between these peaks follows the increase of Sb incorporated in the film, while their intensities weaken (yellow and magenta curves). iii) For the sample with the highest Sb content in the series (blue curve), only the peak at 4.67 $Å^{-1}$ is still visible and is narrower. The mean interplanar distance d_{av}, calculated from the measured position of the 00.15 peak in the scans, [27] is shown in the last column of **Table 1** for the samples which curves have been fitted (see afterwards).

These double peak features are interpreted as a signature of $(Sb_2Te_3)_m(Sb_2)_n$ superstructures in the films. Indeed, as in the case of Sb_2Te_3, a series of satellite peaks along the symmetric rod is expected for a highly periodic stacking. The fact that in the present data only few of these

peaks are visible indicates an irregular mixture of Sb_2Te_3 and Sb DLs in the $Sb_{2+x}Te_3$ films. Similarly to epitaxial $Bi_{2+x}Te_3$ films, [26] the repetition of Sb_2Te_3 and Sb_2 slabs during the growth is slightly inaccurate, resulting in a certain dispersion with respect to the ideally ordered stacking sequence. Still, the information about the average periodicity is preserved. Also, the weakening and broadening of the $(Sb_2Te_3)_m(Sb_2)_n$ superstructure features as a function of the excess of Sb indicate a gradual loss of order in the films. A relation between this observation and the decreasing growth rate in the series, measured by X-ray reflectivity (see Figure S1(a) and Table S1 in supplementary) can be excluded. In fact, very similar results have been obtained in different $Sb_{2+x}Te_3$ series where the Sb flux was increased to provide the Sb excess while keeping the Te flux constant (shown below). The formation of non-continuous Sb_2 DLs as well as of thicker Sb_{2n} blocks can explain the loss of order. Moreover, additional shoulders appear in the samples with higher Sb content (magenta and blue curves), possibly revealing the formation of mixed $Sb_{2+x}Te_3$ phases. The presence of thicker Sb_{2n} blocks or even local Sb segregation cannot be excluded (see discussion in Section 3).

The XRD radial scans of our samples reveal a drastic change in the structure as a function of the excess of Sb. In particular, the highly periodic structure of Sb_2Te_3 is gradually lost. The appearance and change of characteristic features in the curves can be used to obtain information about the composition and structural quality of the alloys. Based on the statistical modeling developed to simulate $Bi_{2+x}Te_3$, [26] we implemented a fit routine for $Sb_{2+x}Te_3$ films. A marked difference with respect to $Bi_{2+x}Te_3$ [28] is that in the present case Sb_{2n} blocks thicker than Sb_2 are likely to form. [17] For simplicity, in the present model we included only Sb_2 and Sb_4 slabs. In the model we assume that the crystal consists of a random sequence of QL-blocks separated by Sb_2 or Sb_4 slabs. The random numbers of QLs in different QL-blocks are statistically independent. The length of the QL sequence between $Sb_2(Sb_4)$ slabs is described in the model by a Gamma distribution. The mean number of QLs in the QL-blocks N_{QL}, its

root-mean square (rms) deviation *width*, as well as the probability p_{Sb4} of finding the Sb_4 slab were used as fitting parameters. Details about the modeling are reported in supplementary information.

The fitted curves are plotted in Figure 2(a) (solid gray lines) along with the experimental ones. The relevant parameters from the fits are collected in Table 1 and S2. We first tested the consistency of the model with Sb_2Te_3 (brown curve in Figure 2(a)). Apart for small discrepancies in the intensity profile, all the features in the radial scan are nicely reproduced. Strikingly, our model allows to track even small deviations from the stoichiometric Sb_2Te_3 composition (see Table 1). Then, we successfully performed the fit for the following two samples in the series (orange and yellow curves). In both cases, the matching between fit and experiment is rather good. The characteristic double features of $Sb_{2+x}Te_3$ alloys as well as their evolution as a function of the excess of Sb are well reproduced. Remarkably, we found that it was not possible to accurately fit the curves when only Sb_2 or Sb_4 slabs are stacked in the films (not shown here). Hence, our data show the coexistence of 1/1 and 2/2 Sb_4Te_3 sequences. Unfortunately, we were not able to fit the curves of the samples richer in Sb. The higher structural disorder, which is responsible for the disappearance of some of the peaks in XRD radial scans, prevents to obtain reliable fits. Moreover, the appearance of additional weak features in the curves may be possibly interpreted as a segregation of different phases, which cannot be reproduced by our model. Therefore, based on these results we can state that only for compositions in between Sb_2Te_3 and SbTe the stacking quality is still not heavily affected.

In a recent paper [29] we studied the epitaxy of GeSbTe alloys on passivated vicinal Si substrates, demonstrating the modulation between vdW and classical epitaxy induced by strain at the Si step edges. Interestingly, the use of miscut substrates also promotes the reduction of the compositional disorder typical of epitaxial GeSbTe. Based on this finding, we repeated the growth of $Sb_{2+x}Te_3$ films on low miscut Si substrates (see Section 6) aiming to

improve the structural quality. Three samples were prepared, intended to have compositions

close to those of the samples labeled with brown (Sb_2Te_3), yellow (SbTe) and magenta (not

fitted) in Figure 2(a). The XRD radial scans of these samples, along with the fitted curve for

each one, are shown in Figure 2(b) (dotted and solid lines, respectively). The XRR

measurements of the samples are shown in the supplementary (Figure S1(b)). The lower

intensity of $Sb_{2+x}Te_3$ peaks with respect to those on normal Si, particularly evident for Sb_2Te_3,

is ascribed to the different thickness between the samples (see Table S1). Remarkably, the

features of $Sb_{2+x}Te_3$ in the radial scans are much sharper (see yellow and magenta curves in

Figure 2(b)). For the latter, a distinct peak at 4.53 Å^{-1} appears, while no additional shoulder is

present. These improvements indicate a significant reduction of the structural disorder and

allowed to fit the curves for all 3 samples (see solid gray lines in Figure 2(b)). In the results

listed in Table S2 the sharper peaks of both yellow and magenta curves are reflected by an

increased ratio of $N_{QL}/width$. Hence, this ratio can be effectively used to evaluate the

structural disorder in $Sb_{2+x}Te_3$ films. For the last sample in the series (magenta) it equals the

value of Sb_2Te_3, while the calculated composition is very close to Sb_4Te_3. Notably, p_{Sb4} is

about 14%, confirming the formation of a mixed Sb_4Te_3 phase with both 1/1 and 2/2 stacking

sequences. Good agreement is found between the film composition values calculated using

our model and those measured by energy dispersive X-ray spectroscopy for the samples

grown on miscut Si(111). These values are reported in the supplementary (Table S3).

Also, in both series p_{Sb4} consistently decreases when more Sb is incorporated. This trend

seems to be counterintuitive; however it can be tentatively explained as follows. When an

exiguous excess of Sb is provided (i.e. for $Sb_{2.72}Te_3$ 3.5 Sb_2Te_3 QLs are in average

sandwiched between Sb_{2n} slabs), the layered nature of Sb_2Te_3 still dominates. Indeed,

although it would in principle be possible to form only Sb_2 DLs, the system preferentially

stacks more consecutive Sb_2Te_3 blocks. As a consequence, in this sample about one quarter of

the Sb layers is doubled (Sb_4). When more Sb is given, instead, this mechanism may be gradually hindered and less Sb_4 slabs are stacked.

3. Raman Spectroscopy

Raman spectroscopy was demonstrated to be suitable to identify the different crystalline phases of GST [30] and to qualitatively access the vertical order in Sb_2Te_3/GeTe(GeSbTe) SLs. [22,31] Interestingly, in the case of $Sb_{2+x}Te_3$ this technique demonstrates excellent sensitivity to the structural changes induced by the excess of Sb, as shown in **Figure 3**(a) for the samples on normal Si. The Raman spectra of the $Sb_{2+x}Te_3$ films grown on miscut substrates are very similar to those on normal Si (see Figure S3(a)). Therefore, while XRD is more powerful in evaluating the structural disorder, Raman scattering allows an estimation of the film composition. Not surprisingly, a red shift of the Sb_2Te_3 modes is clearly present along the series, related to the composition dependent increase of lattice parameters (in Figure S3(b) we plot the position of the $A_{1g}^{(1)}$ and $E_g^{(2)}$ modes for the series on miscut Si). More relevant, the $A_{1g}^{(1)}$ and $E_g^{(2)}$ modes are gradually suppressed, testifying the strong link of these vibrations with the layered structure of Sb_2Te_3, while the $A_{1g}^{(2)}$ one only slightly broadens. In particular the intense $A_{1g}^{(1)}$ mode, which completely vanishes in the last spectrum of the series, is the most affected. Also, new modes appear in the spectra (black arrows). (i) For all the samples with Sb excess (x > 0.7) a peak at ~98 cm^{-1} is visible. (ii) For x ≥ 1 a broad peak centered at ~130 cm^{-1} gradually emerges. (iii) Finally, in the last 2 samples spectra (x ≥ 2) fairly weak modes at about 147 cm^{-1}, 155 cm^{-1} and a shoulder at ~170 cm^{-1} rise.

In order to uncover the structural evolution responsible for the changes measured in the Raman spectra, addressing in particular the origin of the additional modes, phonons at the Γ point and the corresponding Raman tensor are calculated within density functional perturbation theory (DFPT) for the two possible structures of Sb_4Te_3 (1/1 and 2/2). The resulting phonon frequencies are reported in Table S5. Details about the calculations are given

in the experimental section and supplementary. We note that pure Sb also crystallizes in a trigonal structure (two atoms per unit cell) with an E_g mode at 115 cm^{-1} and an A_{1g} mode at 150 cm^{-1} visible in the experimental Raman spectrum [32]. Theoretical calculations for a single self-standing Sb bilayer [33] show that these two modes shift to higher frequency, namely at about 150 cm^{-1} (E_g) and 187 cm^{-1} (A_{1g}).

The theoretical Raman spectra of Sb_4Te_3 obtained for the 1/1 and 2/2 structures are plotted in Figure 3(b), along with that of Sb_2Te_3 from Ref. [34]. Our spectra for Sb_4Te_3 still display an intense peak around 110 cm^{-1} that is found for Sb_2Te_3 and that can be ascribed to the use of non-resonant conditions in our calculation (see supplementary). Therefore, in the comparison with experiments we disregard the intensity of this central peak and consider only the intensity ratio among the other peaks. A detailed description of the theoretical spectra of Sb_4Te_3 is reported in the supplementary. The main features which characterize the spectra are highlighted in Figure 3(b) with squares and circles. The corresponding displacement patterns are shown in Figure 3(c-j). The peaks marked with full and empty squares are A_{1g} modes involving mostly the motion of Sb_2Te_3 layers, which correspond to the two A_{1g} modes of Sb_2Te_3. These modes red shift when Sb DLs are introduced. Full and empty circles indicate, respectively, the E_g and the A_{1g} modes involving only the motion of the Sb bilayers. These correlate with the modes of bulk Sb and single self-standing Sb bilayer. A consistent red shift of both peaks, when increasing the number of Sb bilayers, is shown. Notably, a characteristic peak at about 97 cm^{-1} is present only in the spectrum of the Sb_4Te_3 2/2 structure. This is an E_g mode also localized on Sb_2Te_3, with the two Sb_2Te_3 layers in anti-phase. Therefore, this mode is a signature of adjacent Sb_2Te_3 QLs. In fact, no corresponding mode is found for Sb_4Te_3 (1/1) and Sb_2Te (see supplementary), both having a single Sb_2Te_3 QL in between Sb slabs. For what concerns the comparison with experiments the following comments can be raised. i) Moving from Sb_2Te_3 to Sb_4Te_3 in the 1/1 stacking all modes are red-shifted, in qualitative agreement with experiments. ii) The ratio between the peaks at about 160 and 60 cm^{-1}, which

is larger in Sb_4Te_3 than in Sb_2Te_3, is also reproduced by theory. iii) The agreement with the experimental spectra is overall better for the 2/2 structure, as highlighted in particular by the peak at about 97 cm^{-1} (~98 cm^{-1} in the experiments), which is not present in the theoretical spectrum of the 1/1 structure. However, this does not exclude the presence of both structures in the films. In fact, the broad feature at ~130 cm^{-1} and the peak at 147 cm^{-1} in the experimental spectra could be assigned to a mixture of the mode at 146 cm^{-1} of the 1/1 structure and that at 138 cm^{-1} of the 2/2 structure, the latter eventually shifted to lower frequency possibly because of the coexistence of other structures with thicker Sb_{2n} blocks. iv) The mixing of the modes at 160 cm^{-1} (1/1) and 166 cm^{-1} (2/2) contributes for the most to the red shift and broadening of the $A_{1g}^{(2)}$ mode of Sb_2Te_3 in the experiments. The additional features at about 155 cm^{-1} and 170 cm^{-1}, which are only present in the samples with composition of Sb_4Te_3 and above, could be explained as signatures of the 2/2 (red shifted as that at 138 cm^{-1}) and 1/1 structures, respectively.

Therefore, this interpretation is in agreement with our XRD simulations. Assuming that disorder in the stacking arises in the experimental samples leading to the coexistence of the 1/1 and 2/2 structures, a more compelling qualitative comparison between theory and experiments could be made by averaging the theoretical spectra of the two structures as shown in Figure 3(b) (magenta curve).

4. Electrical Characterization

Table 2 summarizes the room temperature (RT) transport and TE properties of the samples grown on miscut Si(111). In accordance with the works of Takagaki [19] and Kuznetsov [35], the samples have p-type conduction and the hole concentration p is linearly proportional to the excess of Sb in the alloys (see Figure S5). The carrier mobility μ and the thermopower S as a function of the hole concentration are shown in **Figure 4**. The relationship between μ and p is well reproduced by a $\mu \propto p^{-1}$ curve (dashed black line). This is as well in agreement with

the data reported by Kuznetsov, [35] interpreted by the authors as a result of scattering from impurities with concentration equal to that of the holes. We recently found that the intrinsic structural disorder in Sb_2Te_3/GeTe SLs limits the carrier mobility while introducing additional carriers in the material. [22] Native Sb_2Te_3/$Ge_xSb_2Te_{3+x}$ SLs, in which the mitigation of intermixing results in a reduced density of stacking faults, have indeed improved carrier mobility. Accordingly here the structural quality typical of Sb_2Te_3 is gradually affected by the increase of Sb in the material. Therefore, our results emphasize the relationship between structural quality and electrical properties in layered chalcogenides. Since the metallic character of the compounds increases following the excess of Sb, the Seebeck coefficient decreases. The dependence between S and p can be approximated by a $S \propto p^{-2/3}$ curve (dashed gray line). This nicely follows the behavior described by simple models of electron transport for metals or degenerate semiconductors, [36] assuming that the carriers effective mass is independent of the film composition in the investigated range. Comparing our results with those of Poudeu and Kanatzidis, [17] the RT thermopower values of Sb_1Te_1 samples are close to each other, while interestingly that of Sb_4Te_3 is about a factor 3 higher in our case. This is a further indication of the improved structural quality, namely less additional carriers, [22] achieved for epitaxial $Sb_{2+x}Te_3$ on miscut Si substrates. Clearly, the TE properties of alloys richer in Sb are more affected by their structural properties. In the case of $Sb_{2.31}Te_3$, the measured thermopower is slightly lower compared to values reported for Sb_2Te_3 thin films in the literature, [37–39] reflecting the small excess of Sb in the film.

The electrical conductivity σ and the power factor $S^2\sigma$ as a function of the Sb excess are shown in Figure S6. A rather small variation of the electrical conductivity between the studied samples is reported (< 15%), as expected considering the p^{-1} relationship between mobility and hole concentration. This is again in line with the data of Kuznetsov and coworkers, [35] but differs from the results of Poudeu and Kanatzidis [17] where σ was reported to continuously

decrease from Sb_8Te_9 to Sb_2Te. The power factor dependence on the Sb content is mostly dominated by that of the thermopower. It ranges between 160 $\mu Wm^{-1}K^{-2}$ for $Sb_{4.05}Te_3$ and 2.52 $mWm^{-1}K^{-2}$ for $Sb_{2.31}Te_3$. Despite the slight Sb excess, this last value is about 5 and 11 times larger than those reported for Sb_2Te_3 grown by MBE [37] and atomic layer deposition [39] respectively, while it approaches that of Sb_2Te_3 fabricated by nanoalloying method. [38,40] Similar power factor values are also reached for co-evaporated Sb_2Te_3 films. [41–43]

We also performed temperature dependent electrical measurements in the range between 4.5 and 300 K. The electrical resistivity, the hole concentration and the hole mobility for the three samples are shown in **Figure 5**(a-c). The three samples show metallic behavior, as expected. Interestingly, we can distinguish between the behavior of the sample with lower excess of Sb ($Sb_{2.31}Te_3$) and that of the two richer in Sb ($Sb_{3.3}Te_3$ and $Sb_{4.05}Te_3$). In analogy with the results shown for Sb_2Te_3/GeTe(GeSbTe) superlattices, [22] the hole concentration of the latter samples (yellow and magenta) show a very weak temperature dependence (Figure 5(b)). The increase of p with respect to temperature is indeed < 5% and < 2% for $Sb_{3.3}Te_3$ and $Sb_{4.05}Te_3$, respectively. The electrical resistivity and the hole mobility have therefore opposite behaviors (Figure 5(a) and (c)). The temperature coefficients of resistivity (TCR) are 0.55 $\mu\Omega cmK^{-1}$ and 0.42 $\mu\Omega cmK^{-1}$ for $Sb_{3.3}Te_3$ (yellow) and $Sb_{4.05}Te_3$ (magenta), respectively. In the case of $Sb_{2.31}Te_3$, instead, the hole concentration decreases with temperature. While the carrier mobility does not change substantially, the electrical resistivity shows a stronger temperature dependence, still linear. Indeed, the TCR is 0.76 $\mu\Omega cmK^{-1}$. Hence, these data show a clear relationship between the TCR and the film composition (hole concentration). This finding can be tentatively attributed to the larger contribution of carrier-carrier scattering as p increases. The rather small difference in the resistivity values at RT may be related to the actual film thicknesses. [44] However, a detailed study as a function of film composition and thickness is required to address this point.

5. Conclusion and Outlook

In conclusion, we fabricated epitaxial $Sb_{2+x}Te_3$ alloys on Si(111) substrates by means of MBE. A combination of XRD and Raman spectroscopy measurements allows to efficiently determine the composition and structural properties of the material. The simulations we developed for both sets of data give an insight into the intrinsic disorder in our samples with respect to $(Sb_2Te_3)_m(Sb_2)_n$ adaptive natural SLs. Based on the present study, a rapid assessment of the composition of $Sb_{2+x}Te_3$ alloys can be drawn by Raman spectroscopy. The possibility to precisely characterize the structural properties of layered chalcogenides opens the way to systematically study the effects of composition and disorder on their properties, for example the TI ones.

In-plane electrical and TE characterization of the films with compositions close to Sb_2Te_3, SbTe and Sb_4Te_3 at RT is reported. Noteworthy, these data demonstrate the improved TE properties of epitaxial Sb_4Te_3, which are strongly linked to the structural quality achieved in the material. Since some disorder is still present in the samples grown on miscut Si, a further increase of the thermopower may be possibly achieved in highly ordered Sb_4Te_3 superstructures. More promising is the case of $Sb_{2+x}Te_3$ alloys with low excess of Sb ($x < 1$). The scenario is different, yet it closely relates to the structural properties of the material. In fact, while we record thermopower values in line with previous reports, the higher electrical conductivity boosts the power factor in the $mWm^{-1}K^{-2}$ range. Clearly, the present achievement is driven by the relatively high carrier mobility despite the carrier concentration is above 10^{20} cm^{-3}, once more paradigmatic of the interplay between structural and electrical properties in these materials. Moreover, we expect to further enhance the thermopower by accurately reducing the excess of Sb in the film, and thus the density of antisite defects, [40,45] towards the Sb_2Te_3 stoichiometry. In order to keep constant the electrical conductivity, it is necessary to ensure to follow the $\mu \propto p^{-1}$ curve in Figure 4.

13

Concerning PCM applications, the situation is more complex since the memory devices are typically operated in the cross-plane direction. Therefore, considering only the in-plane electrical properties it is not trivial to predict the effect on the switching performance of SL devices. With respect to the alloy composition, the electrical conductivity does not change in our case. This means that the electronic contribution to the in-plane thermal conductivity is also unchanged (Wiedemann-Franz law), while we do not expect additional phonon scattering since the Sb slabs have sub nm size. For the same alloy composition, instead, a reduction of the structural disorder is forecasted to improve the in-plane carrier mobility. [22] Moreover, the material anisotropy becomes larger, possibly affecting the switching. In fact, the heat generated during the device operation would preferentially flow laterally rather than vertically, meaning that a higher power is required to complete the switching. At the same time, however, the more efficient lateral heat flow may favor a faster switching. Also, epitaxial $Sb_{2+x}Te_3$ films are much smoother compared to Sb_2Te_3, as shown in the Supplementary (Figure S1). This as well should play a role in improving the SL structural quality.

As mentioned in the introduction, $Sb_{2+x}Te_3$ alloys were proposed to realize strain engineered phase change SLs, leveraging on the larger lattice parameter. [14] To this end, the present results demonstrate that while the control of the structure of $(Sb_2Te_3)_m(Sb_2)_n$ natural SLs at the nanoscale is fundamental, further effort must be dedicated to the optimization of the material. In fact, the formation of incomplete Sb DLs as well as of thicker Sb blocks which appears from our analysis would hinder the realization of fully coupled heterostructures, reducing the effective strain exerted on the GeTe layers. [12] Ultimately, MBE offers a unique possibility for the growth of $Sb_{2+x}Te_3$ alloys which could potentially be exploited to control at the nanoscale both the stacking sequence and the ordering. The same applies also to other V_2VI_3 chalcogenides. It paves the way for the demonstration of a novel concept in material science, where the strain in the heterostructure can be readily tuned by engineering the number of vdW

gaps per unit thickness, tailoring the V_2VI_3 properties in between those of 2D and 3D

materials.

6. Experimental Section

Sample preparation: $Sb_{2+x}Te_3$ films were fabricated by MBE on Si(111)-(√3 × √3)R30∘-Sb

passivated surfaces. Both normal Si(111) and miscut Si(111) (1° aligned 45° from the in plane

($\overline{1}\overline{1}2$) direction of Si(111)) were used. The latter are also high-resistivity Si (> 5000 Ωcm),

allowing to avoid the contribution of the substrate while measuring lateral electrical transport

properties. The substrate cleaning method and the preparation of the Si(111)-(√3 × √3)R30°-

Sb surface were described by Wang et al.. [46] Starting from stoichiometric Sb_2Te_3, [9] the

composition of $Sb_{2+x}Te_3$ was controlled by increasing the Sb/Te atomic flux ratio, providing

the Sb excess either decreasing the Te flux while keeping fixed the Sb one (series on normal

Si(111)) or vice versa (series on miscut Si(111)). All other growth parameters were

unchanged. The substrate temperature was ~230 °C for all the growths.

X-ray diffraction: The diffractometer used for the XRD and XRR characterization is a

PANalytical X' Pert PRO MRD system with a Ge(220) hybrid monochromator, employing a

CuKα$_1$ (λ = 1.540598 Å) X-ray radiation. The data analysis was carried out using Xrayutilities.
[47]

X-ray diffraction simulation: Details about the modeling are reported in supplementary

information. The main parameters in the model are the average number of Sb_2Te_3 blocks in

between $Sb_2(Sb_4)$ layers (N_{QL}), the ratio between Sb_4 and Sb_2 layers (p_{Sb4}) and the rms

deviation of the number of QLs in the QL-blocks (*width*). The alloy composition can be

directly calculated from the first two parameters, while the third one is an indication of the

dispersion with respect to the average stacking.

Raman spectroscopy: The Raman spectra were acquired in backscattering z(y,xy)-z geometry,

the sample was excited with the 632.8 nm line of a He–Ne laser, and the scattered light was

analyzed using a spectrometer equipped with an liquid N_2-cooled charge-coupled device (CCD) detector. The emission was focused by a microscope objective with 0.9 numerical aperture and the same objective was used for the collection of the signal. The spatial resolution achieved is 0.7 cm^{-1} and a notch filter suppressed the stray light.

Density functional theory calculations: We have optimized the geometry of the Sb_4Te_3 (1/1) and (2/2) structures by means of density functional theory (DFT) calculations using the Quantum-Espresso suite of programs, [48] the Perdew-Burke-Ernzerhof exchange and correlation functional [49] and the van der Waals correction due to Grimme (D2). [50] The optimized lattice parameters are reported in Table S3 for the two structures. The 2/2 structure is lower in energy by 5 meV per atom. This value is compatible with the coexistence of the 2/2 and 1/1 structures observed experimentally. For simplicity we assume here an equal amount of the two phases in the experimental sample. The configurational entropy per 2/2 formula unit associated with a totally random distribution of the 2/2 units can be estimated as $k_B \, 3 \, ln \, 2$, where k_B is the Boltzmann constant. At the temperature of the MBE growths (T ~500 K) the free energy gain per 2/2 formula unit due to configurational entropy is thus $k_B T \, 3 \, ln \, 2 \approx 90 \, meV$, which overcomes the energy difference between the 1/1 and 2/2 phases, amounting to $5 \, meV \cdot 7 \cdot 2 = 70 \, meV$ (per 2/2 formula unit). Hence, the experimentally observed coexistence of the two phases also implies that the vibrational contribution to the free energy does not favor one phase with respect to the other. The theoretical Raman spectra at 300 K are computed within density functional perturbation theory [51] for non-resonant conditions in backscattering geometry along the c axis and for non-polarized light. A Lorenzian broadening of 3 cm^{-1} is assigned to all peaks. The Bose factor is computed at 300 K.

Thermoelectric characterization: Lateral electrical transport properties of $Sb_{2+x}Te_3$ samples were studied by temperature dependent Hall measurements in the range between 4.5 and 300 K. In order to avoid a contribution of the substrate, the 3 samples have been grown on high-

resistivity Si(111) (>5000 Ωcm). A four-contact van der Pauw configuration was realized by wire bonding the samples to the chip carriers using In droplets and Au wires. The measurements were performed applying currents and magnetic fields of 0.5 mA and 0.5 T, respectively. The measurements relative errors are $< 10^{-4}$ and $< 10^{-2}$ for the sheet resistance and the Hall resistance, respectively. The measurements of the Seebeck coefficient were performed on the same 3 samples. A Peltier cooling element was used to apply the temperature gradient (~3°C in 7 steps). Ag conductive paste in between the Peltier element and the sample is needed to improve the thermal contact conductance. The voltage difference was measured in a two-contact configuration.

Supporting Information
Supporting Information is available from the Wiley Online Library or from the author.

References

[1] K. S. Novoselov, A. K. Geim, S. V Morozov, D. Jiang, Y. Zhang, S. V Dubonos, I. V Grigorieva, A. A. Firsov, *Science* **2004**, *306*, 666.

[2] C. Berger, Z. Song, T. Li, X. Li, A. Y. Ogbazghi, R. Feng, Z. Dai, N. Alexei, M. E. H. Conrad, P. N. First, W. a. De Heer, *J. Phys. Chem. B* **2004**, *108*, 19912.

[3] G. Fiori, F. Bonaccorso, G. Iannaccone, T. Palacios, D. Neumaier, A. Seabaugh, S. K. Banerjee, L. Colombo, *Nat. Nanotechnol.* **2014**, *9*, 768.

[4] K. S. Novoselov, D. Jiang, F. Schedin, T. J. Booth, V. V Khotkevich, S. V Morozov, A. K. Geim, *Proc. Natl. Acad. Sci. U. S. A.* **2005**, *102*, 10451.

[5] A. Koma, *Thin Solid Films* **1992**, *216*, 72.

[6] Y. Takagaki, A. Giussani, K. Perumal, R. Calarco, K.-J. Friedland, *Phys. Rev. B* **2012**, *86*, 125137.

[7] R. Simpson, P. Fons, A. Kolobov, T. Fukaya, M. Krbal, T. Yagi, J. Tominaga, *Nat. Nanotechnol.* **2011**, *6*, 501.

[8] R. Venkatasubramanian, E. Siivola, T. Colpitts, B. O'Quinn, *Nature* **2001**, *413*, 597.

[9] J. E. Boschker, J. Momand, V. Bragaglia, R. Wang, K. Perumal, A. Giussani, B. J. Kooi, H. Riechert, R. Calarco, *Nano Lett.* **2014**, *14*, 3534.

[10] J. E. Boschker, L. A. Galves, T. Flissikowski, J. M. J. Lopes, H. Riechert, R. Calarco, *Sci. Rep.* **2015**, *5*, 18079.

[11] S. Cecchi, R. N. Wang, E. Zallo, R. Calarco, *Nanosci. Nanotechnol. Lett.* **2017**, *9*, 1114.

[12] R. Wang, F. R. L. Lange, S. Cecchi, M. Hanke, M. Wuttig, R. Calarco, *Adv. Funct. Mater.* **2018**, *28*, 1705901.

[13] J. Kalikka, X. Zhou, E. Dilcher, S. Wall, J. Li, R. E. Simpson, *Nat. Commun.* **2016**, *7*, 11983.

[14] X. Zhou, J. Kalikka, X. Ji, L. Wu, Z. Song, R. E. Simpson, *Adv. Mater.* **2016**, *28*, 3007.

[15] N. F. Hinsche, B. Y. Yavorsky, I. Mertig, P. Zahn, *Phys. Rev. B - Condens. Matter*

Mater. Phys. **2011**, *84*, 165214.

[16] L. E. Shelimova, O. G. Karpinskii, V. I. Kosyakov, V. A. Shestakov, V. S. Zemskov, F. A. Kuznetsov, *J. Struct. Chem.* **2000**, *41*, 81.

[17] P. F. P. Poudeu, M. G. Kanatzidis, *Chem. Commun.* **2005**, 2672.

[18] T. Valla, H. Ji, L. M. Schoop, A. P. Weber, Z. H. Pan, J. T. Sadowski, E. Vescovo, A. V. Fedorov, A. N. Caruso, Q. D. Gibson, L. Müchler, C. Felser, R. J. Cava, *Phys. Rev. B - Condens. Matter Mater. Phys.* **2012**, *86*, 241101.

[19] Y. Takagaki, A. Giussani, J. Tominaga, U. Jahn, R. Calarco, *J. Phys. Condens. Matter* **2013**, *25*, 345801.

[20] M. Eschbach, M. Lanius, C. Niu, E. Młyńczak, P. Gospodarič, J. Kellner, P. Schüffelgen, M. Gehlmann, S. Döring, E. Neumann, M. Luysberg, G. Mussler, L. Plucinski, M. Morgenstern, D. Grützmacher, G. Bihlmayer, S. Blügel, C. M. Schneider, *Nat. Commun.* **2017**, *8*, 14976.

[21] M. Boniardi, A. Redaelli, I. Tortorelli, S. Lavizzari, A. Pirovano, F. Pellizzer, E. Varesi, D. Erbetta, C. Bresolin, A. Modelli, R. Bez, *2012 4th IEEE Int. Mem. Work. IMW 2012* **2012**, 31.

[22] S. Cecchi, E. Zallo, J. Momand, R. Wang, B. J. Kooi, M. A. Verheijen, R. Calarco, *APL Mater.* **2017**, *5*, 026107.

[23] K. Kifune, Y. Kubota, T. Matsunaga, N. Yamada, *Acta Crystallogr. B.* **2005**, *61*, 492.

[24] T. L. Anderson, H. B. Krause, *Acta Crystallogr. Sect. B Struct. Crystallogr. Cryst. Chem.* **1974**, *30*, 1307.

[25] H. Zhang, Y. Cheng, M. Tang, X. Chen, G. Ji, *Comput. Mater. Sci.* **2015**, *96*, 342.

[26] H. Steiner, V. Volobuev, O. Caha, G. Bauer, G. Springholz, V. Holý, *J. Appl. Crystallogr.* **2014**, *47*, 1889.

[27] G. Springholz, S. Wimmer, H. Groiss, M. Albu, F. Hofer, O. Caha, D. Kriegner, J. Stangl, G. Bauer, V. Holý, *Phys. Rev. Mater.* **2018**, *2*, 054202.

[28] K. Yamana, K. Kihara, T. Matsumoto, *Acta Crystallogr. Sect. B* **1979**, *0505*, 147.

[29] E. Zallo, S. Cecchi, J. E. Boschker, A. M. Mio, F. Arciprete, S. Privitera, R. Calarco, *Sci. Rep.* **2017**, *7*, 1466.

[30] V. Bragaglia, K. Holldack, J. E. Boschker, F. Arciprete, E. Zallo, T. Flissikowski, R. Calarco, *Sci. Rep.* **2016**, *6*, 28560.

[31] E. Zallo, R. Wang, V. Bragaglia, R. Calarco, *Appl. Phys. Lett.* **2016**, *108*, 221904.

[32] X. Wang, K. Kunc, I. Loa, U. Schwarz, K. Syassen, *Phys. Rev. B - Condens. Matter Mater. Phys.* **2006**, *74*, 1.

[33] D. Campi, M. Bernasconi, G. Benedek, *Phys. Rev. B - Condens. Matter Mater. Phys.* **2012**, *86*, 075446.

[34] G. C. Sosso, S. Caravati, M. Bernasconi, *J. Phys. Condens. Matter* **2009**, *21*, 095410.

[35] P. I. Kuznetsov, B. S. Shchamkhalova, V. O. Yapaskurt, V. D. Shcherbakov, V. A. Luzanov, G. G. Yakushcheva, V. A. Jitov, V. E. Sizov, *J. Cryst. Growth* **2017**, *471*, 1.

[36] M. Cutler, J. F. Leavy, R. L. Fitzpatrick, *Phys. Rev.* **1964**, *133*.

[37] Y. Kim, A. DiVenere, G. K. L. Wong, J. B. Ketterson, S. Cho, J. R. Meyer, *J. Appl. Phys.* **2002**, *91*, 715.

[38] M. Winkler, X. Liu, J. D. König, S. Buller, U. Schürmann, L. Kienle, W. Bensch, H. Böttner, *J. Mater. Chem.* **2012**, *22*, 11323.

[39] S. Zastrow, J. Gooth, T. Boehnert, S. Heiderich, W. Toellner, S. Heimann, S. Schulz, K. Nielsch, *Semicond. Sci. Technol.* **2013**, *28*, 035010.

[40] N. Peranio, M. Winkler, Z. Aabdin, J. König, H. Böttner, O. Eibl, *Phys. Status Solidi* **2012**, *209*, 289.

[41] L. M. Goncalves, P. Alpuim, A. G. Rolo, J. H. Correia, *Thin Solid Films* **2011**, *519*, 4152.

[42] J.-H. Kim, J. Choi, J. Bae, M. Kim, T. Oh, *Mater. Trans.* **2013**, *54*, 618.

[43] H. Shen, S. Lee, J. gu Kang, T. Y. Eom, H. Lee, S. Han, *Appl. Surf. Sci.* **2018**, *429*, 115.

[44] N. F. Hinsche, S. Zastrow, J. Gooth, L. Pudewill, R. Zierold, F. Rittweger, T. Rauch, J. Henk, K. Nielsch, I. Mertig, *ACS Nano* **2015**, *9*, 4406.

[45] L. W. Da Silva, M. Kaviany, C. Uher, *J. Appl. Phys.* **2005**, *97*, 114903.

[46] R. Wang, J. E. Boschker, E. Bruyer, D. Di Sante, S. Picozzi, K. Perumal, A. Giussani, H. Riechert, R. Calarco, *J. Phys. Chem. C* **2014**, *118*, 29724.

[47] D. Kriegner, E. Wintersberger, J. Stangl, *J. Appl. Crystallogr.* **2013**, *46*, 1162.

[48] P. Giannozzi, S. Baroni, N. Bonini, M. Calandra, R. Car, C. Cavazzoni, D. Ceresoli, G. L. Chiarotti, M. Cococcioni, I. Dabo, A. Dal Corso, S. de Gironcoli, S. Fabris, G. Fratesi, R. Gebauer, U. Gerstmann, C. Gougoussis, A. Kokalj, M. Lazzeri, L. Martin-Samos, N. Marzari, F. Mauri, R. Mazzarello, S. Paolini, A. Pasquarello, L. Paulatto, C. Sbraccia, S. Scandolo, G. Sclauzero, A. P. Seitsonen, A. Smogunov, P. Umari, R. M. Wentzcovitch, *J. Phys. Condens. Matter* **2009**, *21*, 395502.

[49] J. P. Perdew, K. Burke, M. Ernzerhof, *Phys. Rev. Lett.* **1996**, *77*, 3865.

[50] S. Grimme, *J. Comput. Chem.* **2006**, *27*, 1787.

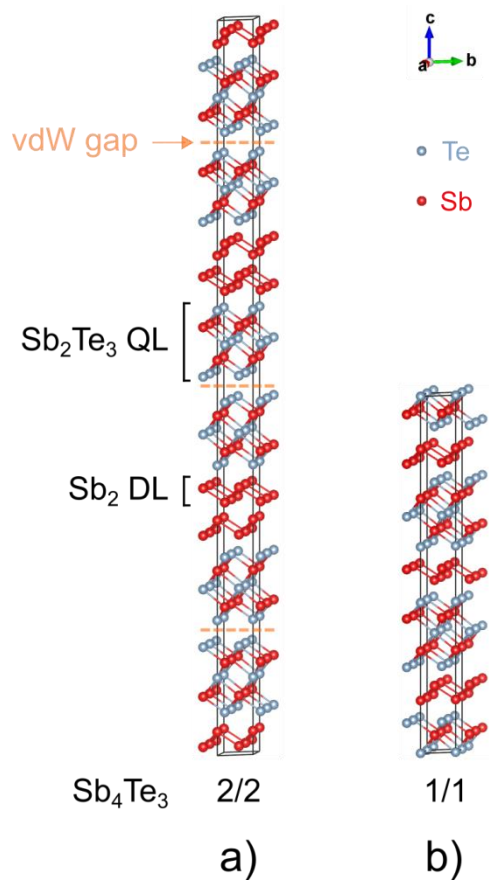[51] S. Baroni, S. De Gironcoli, A. Dal Corso, P. Giannozzi, *Rev. Mod. Phys.* **2001**, *73*, 515.

Figure 1: Sb_4Te_3 2/2 (a) and 1/1 (b) structures optimized by density functional theory calculations (see Section 6).
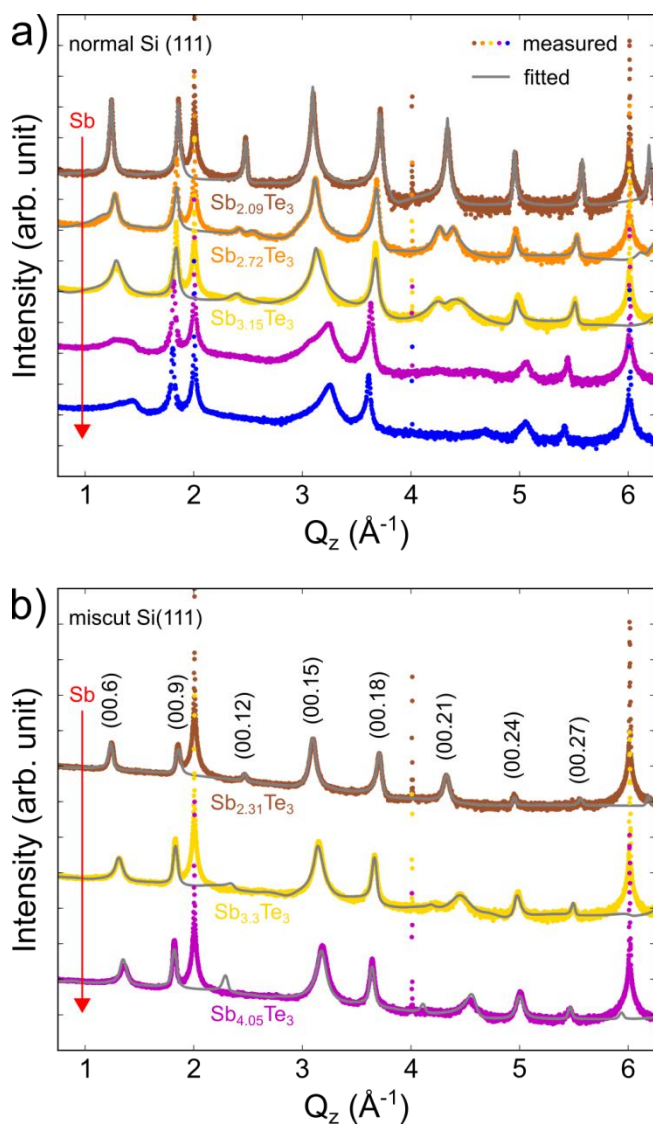
Figure 2: XRD radial scans of Sb$_{2+x}$Te$_3$ samples grown on (a) normal Si(111) and (b) miscut Si(111). Sb$_2$Te$_3$ curves are plotted in brown, while orange, yellow, magenta and blue curves correspond to Sb-rich samples with increasing excess of Sb. The curves are plotted in logarithmic scale and vertically shifted for clarity. The fitted curves (solid gray lines) are superposed to the measurements. The alloy compositions, as calculated from the fits, are also shown. The sharp peaks at ~2, 4 and 6 Å^{-1} correspond to the (111), (222), and (333) Bragg reflections of the Si substrate. Sb$_2$Te$_3$ symmetric Bragg reflections are labeled in (b). The red arrows indicate the increase of Sb in the 2 series.
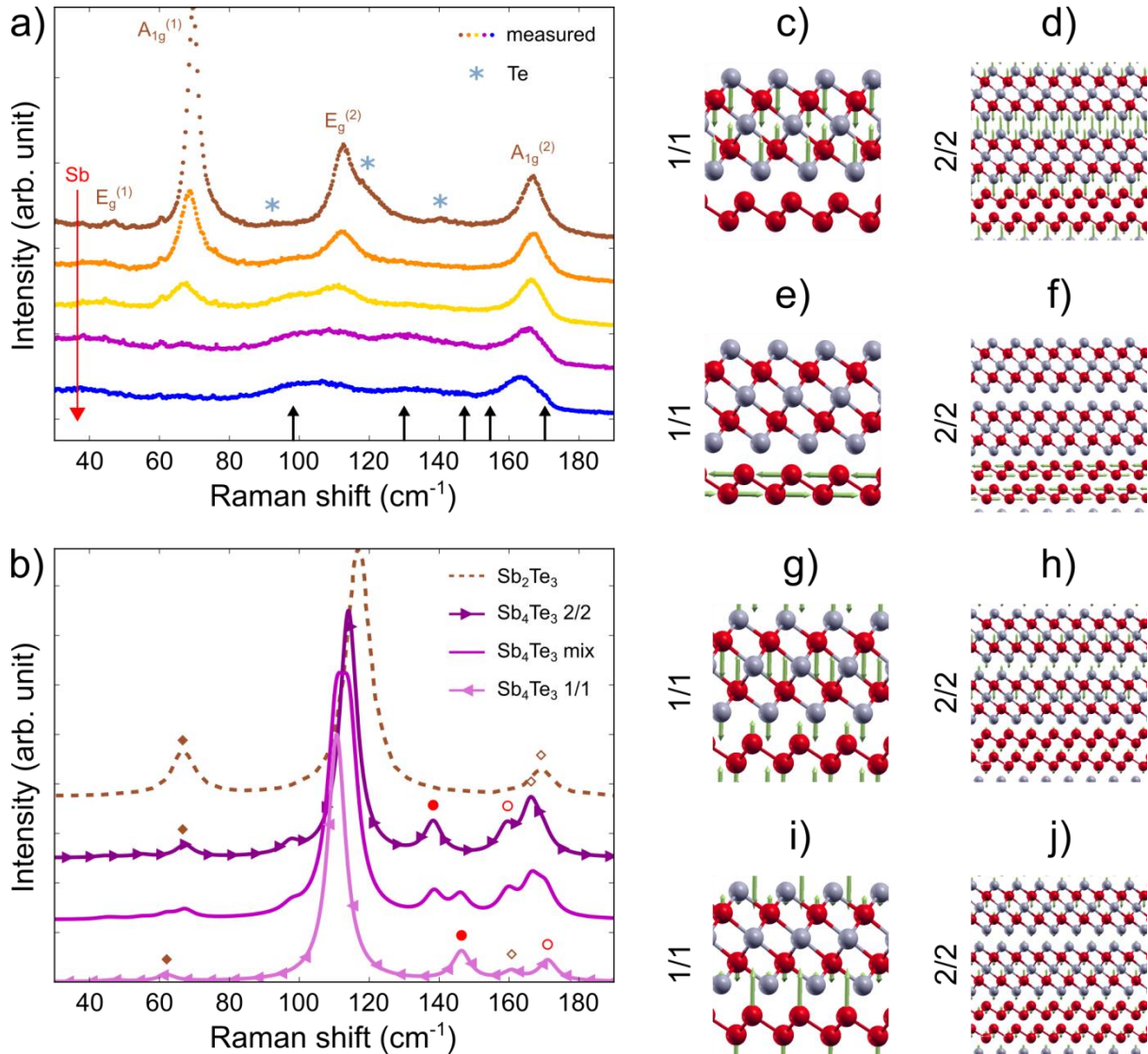
Figure 3: (a) Raman spectra of $Sb_{2+x}Te_3$ samples grown on normal Si(111). $Sb_{2.09}Te_3$ curve is plotted in brown (the modes of Sb_2Te_3 are also labeled), while orange ($Sb_{2.72}Te_3$), yellow ($Sb_{3.15}Te_3$), magenta and blue curves correspond to Sb-rich samples with increasing excess of Sb (see red arrow). The curves are vertically shifted for clarity. The black arrows indicate the features appearing in $Sb_{2+x}Te_3$ samples. The weak peaks at about 92, 119 and 140 cm^{-1} visible in the spectrum of Sb_2Te_3 (gray markers) are a signature of the presence of few Te segregated in the sample, as clarified in Figure S4. (b) Theoretical Raman spectra for Sb_4Te_3 in the 1/1 and 2/2 structures, violet and purple curves with left and right triangle markers respectively, along with that of Sb_2Te_3 from the paper of Sosso et al., [34] dashed brown curve. The theoretical Sb_4Te_3 spectrum averaged over the 1/1 and 2/2 spectra is also shown (magenta curve). The spectra are normalized to the intensity of the peaks at about 110 cm^{-1} and vertically shifted for clarity. (c-j) Displacement patterns of relevant modes of Sb_4Te_3 for the 1/1 (c,e,g,i) and 2/2 (d,f,h,j) structures; Displacement patterns of the A_{1g} mode at (c) 62 cm^{-1} in the 1/1 structure and (d) 67 cm^{-1} in the 2/2 structure (highlighted in (b) with full brown squares); Displacement patterns of the E_g modes due to the Sb layers at (e) 146 cm^{-1} in the 1/1 structure and (f) 138 cm^{-1} in the 2/2 structure (highlighted in (b) with full red circles); Displacement patterns of the A_{1g} mode at (g) 160 cm^{-1} in the 1/1 structure and (h) 166 cm^{-1} in the 2/2 structure mostly localized on the Sb_2Te_3 layers (highlighted in (b) with empty brown squares); Displacement patterns of the A_{1g} mode at (i) 171 cm^{-1} in the 1/1 structure and (j) 159

cm^{-1} in the 2/2 structure mostly localized on the Sb bilayers (highlighted in (b) with empty red circles).
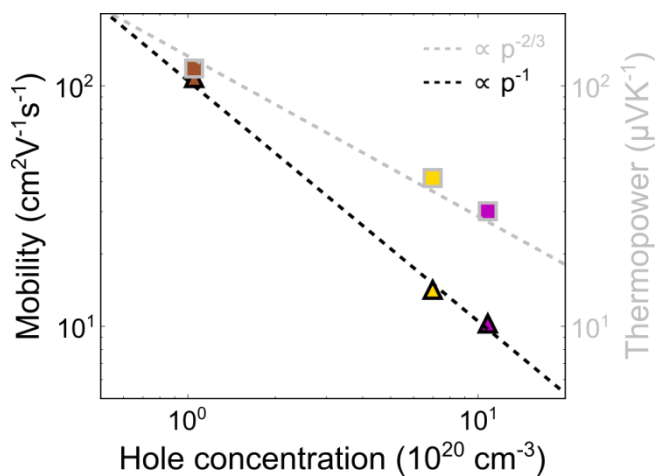

Figure 4: RT carrier mobility (triangles with black border) and thermopower (squares with gray borders) as a function of the hole concentration of the Sb$_{2+x}$Te$_3$ films grown on miscut Si. The black and gray dashed lines are a $k_\mu p^{-1}$ curve with $k_\mu = 1.05 \times 10^2$ cm^{-1}V^{-1}s^{-1} and a $k_S p^{-2/3}$ curve with $k_S = 1.33 \times 10^2$ cm^{-2}μVK^{-1}, respectively. Both curves are meant to be guide to the eyes.
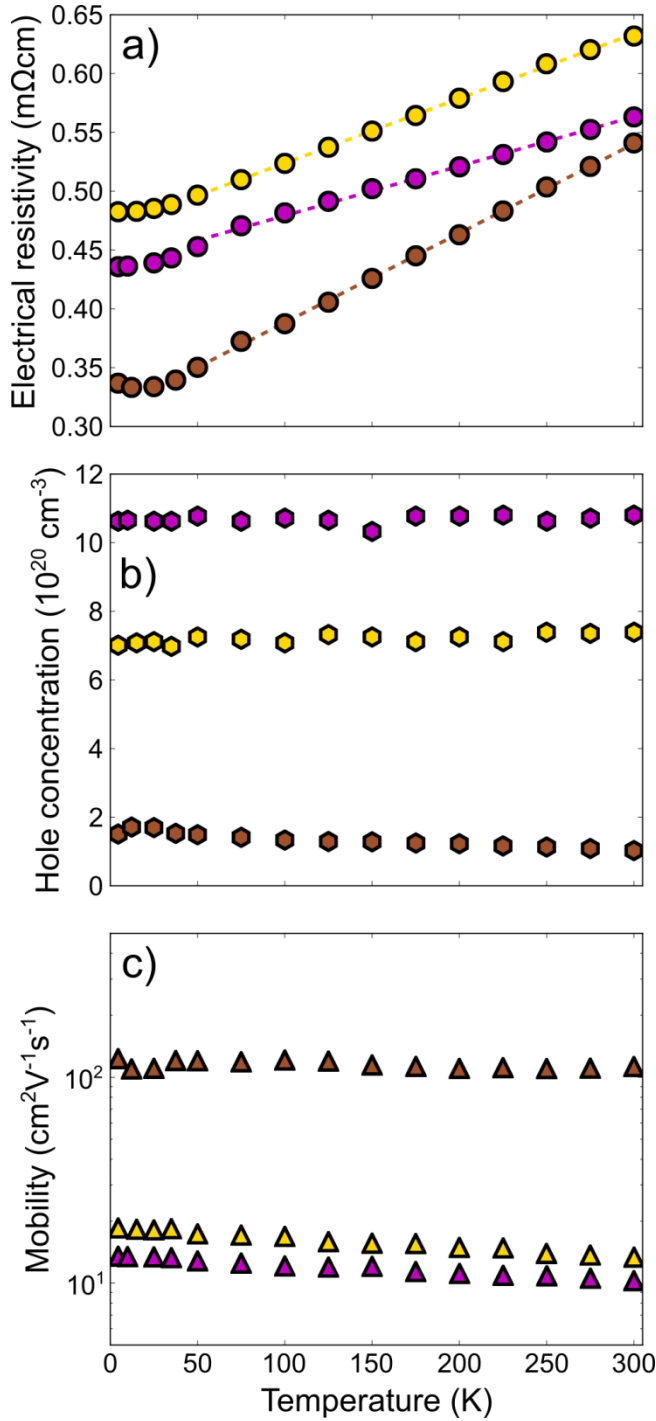
Figure 5: Temperature dependent electrical measurements of the $Sb_{2+x}Te_3$ films grown on miscut Si. $Sb_{2.31}Te_3$, $Sb_{3.3}Te_3$ and $Sb_{4.05}Te_3$ are plotted in brown, yellow and magenta, respectively. (a) The electrical resistivity, (b) the hole concentration and (c) the hole mobility are plotted as a function of the temperature in the range between 4.5 and 300 K. The TCR is defined as the slope of the dashed lines in (a) calculated between 50 K and 300 K.

Table 1. Relevant parameters fitted for $Sb_{2+x}Te_3$ samples on normal and miscut Si. Those grown on miscut Si are marked with an asterisk. The N_{QL} parameter is the average number of Sb_2Te_3 blocks in between $Sb_2(Sb_4)$ layers, *width* is its rms deviation, while p_{Sb4} is the ratio between Sb_4 and Sb_2 slabs. Statistical errors for N_{QL}, *width* and p_{Sb4}, obtained from the least

squares optimization, are below 5% of the respective value. The mean interplanar distance d_{av} is shown in the last column.

Sample composition	N_{QL} [# QLs]	width [# QLs]	p_{Sb4} [%]	d_{av} [Å]
$Sb_{2.09}Te_3$	24.7	12.2	21	2.03
$Sb_{2.72}Te_3$	3.5	2.2	25	2.02
$Sb_{3.15}Te_3$	2.0	1.8	18	2.00
$Sb_{2.31}Te_3$*	9.4	5.1	77	2.03
$Sb_{3.3}Te_3$*	1.7	1.0	22	2.00
$Sb_{4.05}Te_3$*	1.0	0.5	14	1.97

Table 2. Transport and TE properties of $Sb_{2+x}Te_3$ samples at 300 K. The hole concentration p, the carrier mobility μ, the thermopower S, the electrical conductivity σ and the power factor PF are reported.

Sample composition	p [10^{20} cm^{-3}]	μ [cm^{2}V^{-1}s^{-1}]	S [μVK^{-1}]	σ [10^3 Scm^{-1}]	PF [mWm^{-1}K^{-2}]
$Sb_{2.31}Te_3$*	1.05	107.44	118	1.81	2.52
$Sb_{3.3}Te_3$*	6.98	14.17	41	1.58	0.35
$Sb_{4.05}Te_3$*	10.80	10.26	30	1.78	0.16

The precise tuning of the properties of epitaxial $Sb_{2+x}Te_3$ in between those of two dimensional and three dimensional materials is established. It paves the way to expand the horizon of strain engineering in phase change memory superlattice structures. The interplay between structural and thermoelectric properties in these alloys is presented.

Van der Waals epitaxy

S. Cecchi*, D. Dragoni, D. Kriegner, E. Tisbi, E. Zallo, F. Arciprete, V. Holy, M. Bernasconi, R. Calarco

Interplay between Structural and Thermoelectric Properties in Epitaxial $Sb_{2+x}Te_3$ Alloys
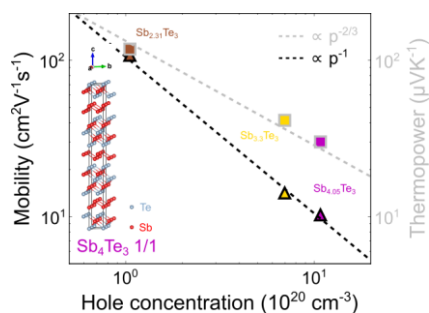
Supporting Information

Interplay between Structural and Thermoelectric Properties in Epitaxial Sb$_{2+x}$Te$_3$ Alloys

Stefano Cecchi*, Daniele Dragoni, Dominik Kriegner, Elisa Tisbi, Eugenio Zallo, Fabrizio Arciprete, Vaclav Holy, Marco Bernasconi, Raffaella Calarco

1. X-ray Reflectivity

The XRR data of the Sb$_{2+x}$Te$_3$ samples on normal and miscut Si are plotted in Figure S1. The film thickness and the root-mean-square (rms) surface roughness have been obtained by fitting the reflectivity curves (these values are reported in Table S1). As shown by Cecchi et al., [1] the surface of epitaxial Sb$_2$Te$_3$ films on Si(111) is relatively rough, a consequence of the nucleation of Sb$_2$Te$_3$ domains which then coalesce forming a continuous film with smooth terraces and quintuple layer (QL) thick steps. Interestingly, the excess of Sb promotes a smoothening of the film surface which can be nicely followed by XRR. Pronounced thickness oscillations in the all measurement range can be seen for Sb$_{2+x}$Te$_3$ samples with $x > 1$ (see yellow and magenta curves). This effect may be directly related to the presence of Sb$_{2n}$ blocks, which effectively diversifies the characteristic surface step structures, as reported for epitaxial Bi$_{2+x}$Te$_3$ films. [2] Also, considering that Sb is a well known surfactant, [3–6] it could alter the nucleation of Sb$_{2+x}$Te$_3$ from the very beginning. However, a conclusive understanding of this aspect requires dedicated experiments, which are not the focus of the present study. The roughness slightly increases for the samples with highest Sb content (blue curve), possibly related to a tradeoff between the beneficial excess of Sb and the growth conditions (namely fluxes ratio and growth rate). On miscut Si the surface roughness follows a trend similar to that observed for Sb$_{2+x}$Te$_3$ films on normal Si. The slight reduction of the roughness with respect to the films grown on normal Si is promoted by the miscut substrate. [7]

Table S1: Film thickness, growth rate and rms surface roughness of $Sb_{2+x}Te_3$ samples. Those grown on miscut Si are marked with an asterisk. The average alloy composition as calculated from the X-ray diffraction (XRD) fits is reported when available. Statistical errors for the estimated film thickness and rms roughness are below 0.3 nm.

Sample composition	Thickness [nm]	Growth rate [nm/min]	rms roughness [nm]
$Sb_{2.09}Te_3$	61.4	0.51	2.9
$Sb_{2.72}Te_3$	50.7	0.42	1.6
$Sb_{3.15}Te_3$	47.9	0.40	1.1
$Sb_{2+x}Te_3$	45.6	0.38	1.3
$Sb_{2+x}Te_3$	39.2	0.32	1.2
$Sb_{2.31}Te_3$*	25.1	0.28	2.6
$Sb_{3.3}Te_3$*	29.1	0.32	0.8
$Sb_{4.05}Te_3$*	33.5	0.37	0.9

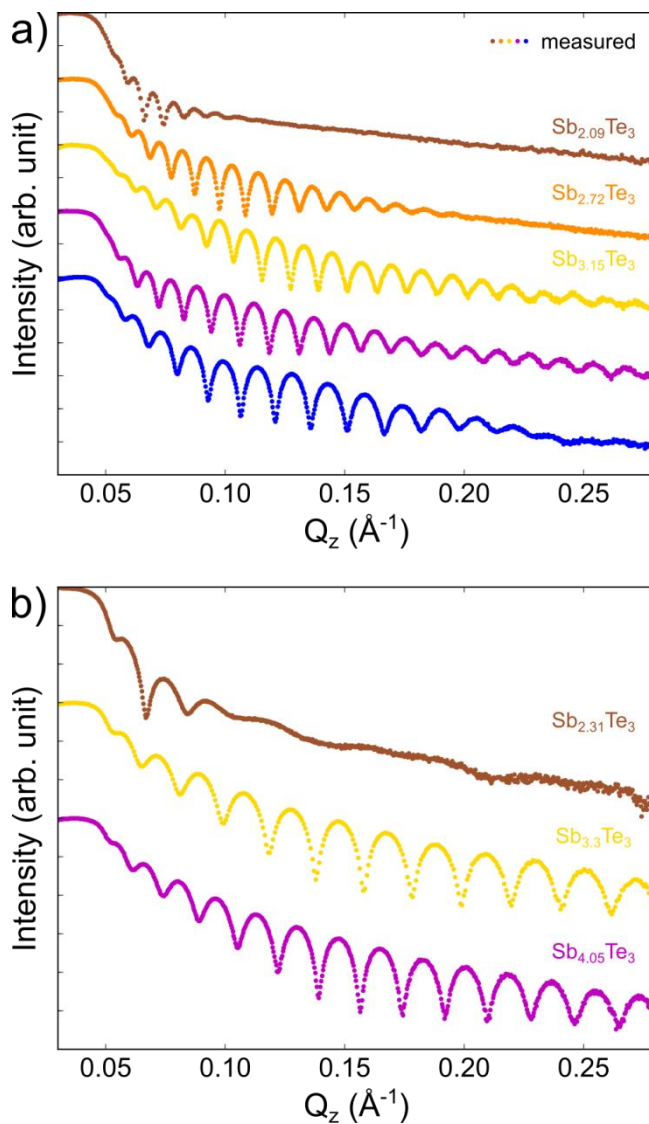**Figure S1**: XRR measurements of $Sb_{2+x}Te_3$ samples grown on (a) normal Si(111) and (b) miscut Si(111). Sb_2Te_3 curves are plotted in brown, while orange, yellow, magenta and blue curves correspond to Sb-rich samples with increasing excess of Sb. The curves are vertically shifted for clarity.

30

2. X-ray Diffraction Simulations

Our simulations of the diffraction signal of the $Sb_{2+x}Te_3$ thin films are based on the kinematical theory description of random chains of QL and Sb_2 or Sb_4 sequences. The diffraction intensity is thereby calculated in complete analogy to equations 15 and 16 in the work of Steiner et al.. [2] The description of the different building blocks thereby considers the following spacing of atomic planes: 1) d_1: distance of the Te-Te layers in a van der Waals (vdW) gap between two QLs; 2) d_2: distance of the Te-Sb layers adjacent to a vdW gap in a QL; 3) d_3: distance of the middle Sb-Te layers in a QL surrounded by other QLs; 4) d_4: distance of the second Sb-Te layers in a QL adjacent to the Sb-Sb double layer (DL); 5) d_5: distance of the Sb-Te layers in a QL adjacent to the Sb-Sb DL; 6) d_6: distance of the last Te layer in a QL from the first Sb layer in a DL; 7) d_7: distance between the layers in a Sb-Sb DL; 8) d_8: distance between two Sb-Sb DLs. Three scenarios visualizing the atomic spacing are given in Figure S2(a-c).

To describe our sample structure we assume that there is a number of QLs ≥ 1 between two Sb building blocks. The number of QLs is assumed to follow a Gamma distribution with parameters 'N_{QL}' and '*width*'. The Sb building block can either be a Sb-Sb DL or with a propability of 'p_{Sb4}' also a stack of two such DLs, i.e. 4 Sb layers. Using the atomic plane distance d_1 to d_8, the statistical parameters described in this paragraph, as well as scaling parameters for primary beam intensity and background we fit the model curves to our experimental data.
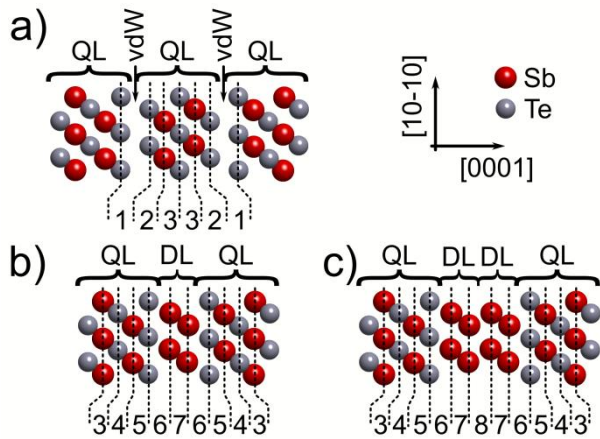
Figure S2: Sketch of the atomic structure of building blocks of $Sb_{2+x}Te_3$. Panel (a) shows the atomic arrangement in a stack of multiple quintuple layers (QLs) as they appear in the Sb_2Te_3 phase. (b) and (c) show the inclusion of Sb-Sb double layers (DLs) between QLs. In all panels the numbers of 1-8 correspond to the atomic spacings d_{1-8} used in the simulations.

The relevant parameters from the fits are collected in Table S2.

Table S2: Relevant parameters fitted for $Sb_{2+x}Te_3$ samples on normal and miscut Si. Those grown on miscut Si are marked with an asterisk. Statistical errors for N_{QL}, *width* and p_{Sb4}, obtained from the least squares optimization, are below 5% of the respective value.

Sample composition	N_{QL} [# QLs]	width [# QLs]	N_{QL}/width [1]	p_{Sb4} [%]
$Sb_{2.09}Te_3$	24.7	12.2	2.0	21
$Sb_{2.72}Te_3$	3.5	2.2	1.6	25
$Sb_{3.15}Te_3$	2.0	1.8	1.1	18
$Sb_{2.31}Te_3$*	9.4	5.1	1.8	77
$Sb_{3.3}Te_3$*	1.7	1.0	1.7	22
$Sb_{4.05}Te_3$*	1.0	0.5	2.0	14

3. Energy dispersive X-ray spectroscopy

Energy dispersive X-ray spectroscopy (EDX) measurements were performed for the $Sb_{2+x}Te_3$ samples grown on miscut Si(111). These were performed in a scanning electron microscope using 6, 8, and 10 keV beam energy of the electrons. The recorded emission spectra contain the K-line of the Si substrate and the L lines of Sb and Te (not shown). The quantification of the composition of the thin films was performed using the STRATAGem software from SAMx. [8] Combining the spectroscopic data of the three excitation energies and using the known energy dependence of fluorescence intensities an error between 1 and 2 at.% is achieved. In Table S3 the film composition values measured by EDX are compared with those

calculated from the XRD fits. There is a general good agreement between EDX and XRD

composition values, the last ones being at the upper part of the given EDX compositional

range.

Table S3: Film composition values measured by EDX of the $Sb_{2+x}Te_3$ samples grown on miscut Si(111). The compositional range is calculated with an error of 1 at.%.

Sample composition (XRD)	Sample composition (EDX with ±1 at.%)
$Sb_{2.?}Te_3$	$Sb_{2.16-2.35}Te_3$
$Sb_{3.3}Te_3$	$Sb_{3.07-3.3}Te_3$
$Sb_{4.05}Te_3$	$Sb_{3.56-3.86}Te_3$

4. Raman Spectroscopy

The Raman spectroscopy data of the $Sb_{2+x}Te_3$ samples grown on miscut Si(111) are shown in

Figure S3(a). We found qualitatively no difference between these spectra and those of

$Sb_{2+x}Te_3$ alloys on normal Si (Figure 3(a)). The spectrum of $Sb_{2.31}Te_3$ is very similar to that of

$Sb_{2.09}Te_3$, although the slight excess of Sb in the film. The Raman shift of the $A_{1g}^{(1)}$ and $E_g^{(2)}$

modes as a function of the excess of Sb in the films is plotted in Figure S3(b), black and gray

respectively. The red shift for the $A_{1g}^{(2)}$ mode (not shown) is within 1%, again highlighting

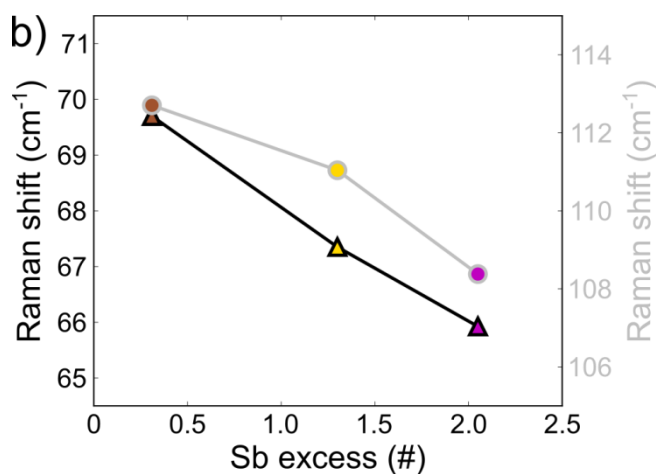the weaker link between this mode and the film composition.
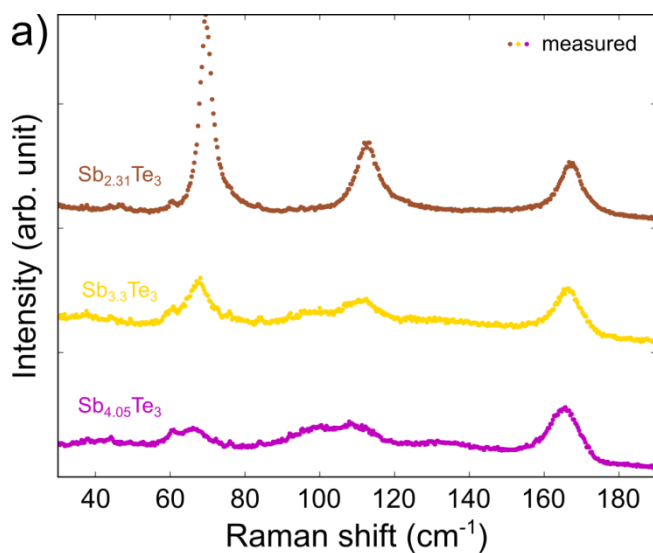
Figure S3: (a) Raman spectra of $Sb_{2+x}Te_3$ samples grown on miscut Si(111). $Sb_{2.31}Te_3$, $Sb_{3.3}Te_3$ and $Sb_{4.05}Te_3$ curves are plotted in brown, yellow and magenta respectively. The curves are vertically shifted for clarity. (b) Raman shift of the $A_{1g}^{(1)}$ (black) and $E_g^{(2)}$ (gray) modes as a function of the excess of Sb in the films.

The Raman spectrum of the $Sb_{2.09}Te_3$ sample shown in Figure 3(a) is compared with those of a reference Sb_2Te_3 [9] and a Sb_2Te_3 sample with strong excess of Te (see Figure S4). The formation of Te segregated in the samples is at the origin of the peaks at 92, 119 and 140 cm^{-1}.

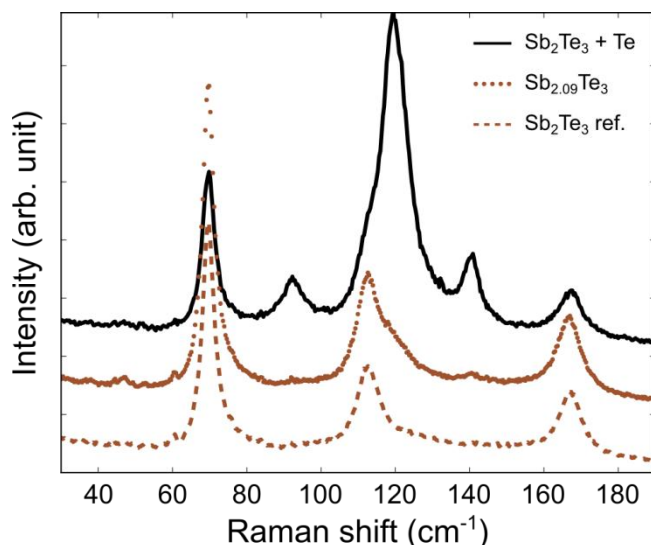**Figure S4:** Raman spectra of $Sb_{2.09}Te_3$ (dotted brown), a reference Sb_2Te_3 (dashed brown) and a Sb_2Te_3 with Te segregated (solid black). All the samples are grown on normal Si(111). The curves are vertically shifted for clarity.

5. Density Functional Theory Calculations

The optimized lattice parameters of the two possible structures of Sb_4Te_3 (1/1 and 2/2), calculated within density functional theory (DFT), are reported in Table S4.

Table S4: Theoretical equilibrium lattice parameters (hexagonal notation). The experimental data of Ref. [10,11] are also reported.

Structure	Functional	a(Å)	c(Å)
1/1	PBE+D2	4.260	41.012
2/2	PBE+D2	4.252	82.591
2/2	Exp.	4.271(1)	83.564(2)

6.Density Functional Perturbation Theory Calculations

The phonon frequencies at the Γ point are calculated for the two relaxed structures within density functional perturbation theory (DFPT). Since the system is actually slightly metallic we did not include the non-analytical contribution to the dynamical matrix giving rise to LO-TO splittings. We computed the Raman cross section by finite differences (0.01 Å) of the susceptibility tensor with respect to the atomic displacement according to Equations 7 and 8 in Ref. [12] to which we refer for all details.

We considered back-scattering geometry with non-polarized light. The same scheme was used for the calculation of the Raman spectrum of Sb_2Te_3 in Ref. [12] (also shown in Figure 3(b)). The theoretical spectrum Sb_2Te_3 is in a good agreement with experiments in the position of the peaks, but the intensity of the peak at 117 cm^{-1} (E_g mode) is largely overestimated in the theoretical spectrum. Such discrepancy can be attributed to the non-resonant condition which is assumed in our theoretical approach as opposed to the resonant condition that actually occurs in experiments. The peaks at 67 and 169 cm^{-1} in Sb_2Te_3 are due to A_{1g} modes.

6.1. Sb_4Te_3

The phonon frequencies at the Γ point, calculated for the two relaxed structures within DFPT, are reported in Table S5.

Table S5: Calculated optical phonon frequencies (cm^{-1}) at the Γ point for the 1/1 and 2/2 structures. All u modes are IR active and all g modes are Raman active. The substructures of the crystal (Sb or Sb_2Te_3 layers) over which phonons are mostly localized are given in the last column (Loc.). The modes with mixed character involve equally the Sb and Sb_2Te_3 layers.

1/1 ω (cm^{-1})	Loc.	2/2 ω (cm^{-1})	Loc.
31 - E_u	+Sb, −Sb_2Te_3	17 - E_g	Sb_2Te_3
38 - A_{2u}	+Sb, −Sb_2Te_3	23 - E_u	Sb
46 - E_g	Sb_2Te_3	24 - A_{1g}	Sb_2Te_3
62 - A_{1g}	Sb_2Te_3	27 - A_{2u}	+Sb, −Sb_2Te_3
92 - E_u	Sb_2Te_3	44 - E_g	mixed
102 - E_u	Sb_2Te_3	45 - E_u	Sb_2Te_3
110 - A_{2u}	Sb_2Te_3	49 - E_g	mixed
110 - E_g	Sb_2Te_3	54 - A_{1g}	+Sb, −Sb_2Te_3
146 - E_g	Sb_2Te_3	61 - A_{2u}	Sb_2Te_3
146 - E_g	Sb	67 - A_{1g}	−Sb, +Sb_2Te_3
160 - A_{1g}	−Sb, +Sb_2Te_3	86 - E_u	Sb_2Te_3
171 - A_{1g}	Sb	97 - E_g	Sb_2Te_3
-		99 - E_u	Sb_2Te_3
-		103 - E_g	Sb_2Te_3
-		112 - A_{2u}	Sb_2Te_3
-		114 - E_g	Sb_2Te_3
-		114 - E_u	Sb_2Te_3
-		115 - A_{1g}	Sb_2Te_3
-		138 - E_g	Sb
-		149 - A_{2u}	Sb_2Te_3
-		150 - E_u	Sb
-		159 - A_{1g}	+Sb, −Sb_2Te_3
-		166 - A_{1g}	mixed, −Sb, +Sb_2Te_3
-		166 - A_{2u}	−Sb, +Sb_2Te_3
-		169 - A_{1g}	mixed
-		170 - A_{2u}	Sb

In the theoretical spectra of Sb_4Te_3 we can identify five main features as detailed below. i) The peaks at 62 cm^{-1} (1/1) and 67 cm^{-1} (2/2) which are due to an A_{1g} mode involving mostly the Sb_2Te_3 layers correspond to the theoretical mode at 67 cm^{-1} of the Sb_2Te_3 crystal. [12] The displacement patterns of these modes, highlighted in Figure 3(b) with full brown squares, are shown in Figure 3(c and d). ii) The peak at about 110 cm^{-1} (1/1) and 114 cm^{-1} (2/2) is an E_g mode involving mostly the motion of the Sb_2Te_3 layers which directly relates to the theoretical mode at 117 cm^{-1} of the Sb_2Te_3 crystal. [12] iii) The peak at about 97 cm^{-1} (2/2) is also an E_g mode localized on Sb_2Te_3 with the two Sb_2Te_3 layers in anti-phase, opposite to the E_g mode at 114 cm^{-1} where the two Sb_2Te_3 layers oscillate in phase. This mode can be seen as a mixture of the $E_u^{(2)}$ and $E_u^{(3)}$ at the zone boundary along c of the Sb_2Te_3 crystal (see Figures 3 and 4 in Ref. [12]). No corresponding mode is found for Sb_4Te_3 (1/1) and Sb_2Te, both having a single Sb_2Te_3 QLs in between Sb slabs. Therefore, this mode is a signature of adjacent Sb_2Te_3 QLs characteristic of the Sb_4Te_3 2/2 structure. iv) The peak at 146 cm^{-1} in the 1/1 structure is due to an E_g mode involving only the motion of the Sb bilayers (see Figure 3(e and f)) which correlates with the E_g mode of the single self-standing bilayer at 150 cm^{-1}. This peak shifts to 138 cm^{-1} in the 2/2 structure which displays two bilayers. This peak, highlighted in Figure 3(b) with full red circles, consistently moves closer to the Sb bulk-like value of 115 cm^{-1} for the E_g mode when increasing the number of Sb bilayers. v) In Sb_4Te_3 we observe a splitting of the peak at 169 cm^{-1} of Sb_2Te_3 into a doublet at 160-171 cm^{-1} (1/1) and 159-166 cm^{-1} (2/2) due to two A_{1g} modes. The peak at 171 cm^{-1} (1/1) is an A_{1g} mode involving the motion of the Sb bilayer which corresponds to the mode at 185 cm^{-1} of the self-standing Sb bilayer. This mode evolves into that at 159 cm^{-1} in the 2/2 structure, moving closer to the A_{1g} mode of bulk Sb at 150 cm^{-1}. This mode is highlighted in Figure 3(b) with empty red circles. The modes at 160 cm^{-1} (1/1) and 166 cm^{-1} (2/2), highlighted in Figure 3(b) with empty brown squares, involve mostly the motion of the Sb_2Te_3 layers with a partial mixing with the motion of the Sb layers (see Figure 3 (g-j)). These correspond to the 169 cm^{-1} mode of pure Sb_2Te_3

which consistently shifts to higher frequency by increasing the number of QLs in between Sb_{2n} slabs.

6.2. Sb_2Te

The crystal structure of Sb_2Te belongs to the *P-3m1* space group as suggested by Agafonov. [13] It can be described by a stacking of two Sb_2 layers and a single Sb_2Te_3 layer along the *c* axis of the standard hexagonal cell. The cell contains 9 atoms whose positions are given in Ref. [13] along with the cell parameters.

We have performed on this structure DFT and DFPT calculations as those described for Sb_4Te_3. The initial structure with atomic positions was taken from Ref. [13] and then fully relaxed. The optimized lattice parameters, calculated within DFT, are reported in Table S6.

Table S6: Theoretical equilibrium lattice parameters for Sb_2Te (hexagonal cell) obtained by DFT-PBE calculations or by adding vdW corrections (PBE+D2). Experimental data from Ref. [13] are also reported.

Functional	a(Å)	c(Å)
PBE	4.348	17.628
PBE+D2	4.266	17.273
Exp.	4.272(1)	17.633(3)

The phonon frequencies at the Γ point are calculated for the relaxed structure within DFPT. The results are reported in Table S7.

Table S7: Calculated optical phonon frequencies (cm^{-1}) at the Γ point for Sb_2Te with PBE+D2 functional. All *u* modes are IR active and all *g* modes are Raman active. The substructures of the crystal (Sb or Sb_2Te_3 layers) over which phonons are mostly localized are given in the last column (Loc.). Some modes with mixed character involve equally the Sb and Sb_2Te_3 layers.

ω (cm⁻¹)	Loc.
PBE+D2	
$28 - E_u$	$+Sb, -Sb_2Te_3$
$34 - A_{2u}$	$+Sb, -Sb_2Te_3$ mixed
$42 - E_g$	mixed
$52 - A_{1g}$	$+Sb, -Sb_2Te_3$
$53 - E_g$	mixed
$67 - A_{1g}$	Sb_2Te_3
$96 - E_u$	Sb_2Te_3
$103 - E_u$	Sb_2Te_3
$106 - E_g$	Sb_2Te_3
$112 - A_{2u}$	Sb_2Te_3
$135 - E_g$	Sb
$144 - A_{2u}$	Sb_2Te_3
$149 - E_u$	Sb
$155 - A_{1g}$	mixed
$165 - A_{1g}$	mixed
$169 - A_{2u}$	Sb

7. Electrical Characterization

The linear relationship between the hole concentration and the excess of Sb in the $Sb_{2+x}Te_3$

alloys is shown in Figure S5. Please note that the linear fit (dashed black) is meant as guide to

the eyes, while a more accurate fit would require measurements of a stoichiometric Sb_2Te_3
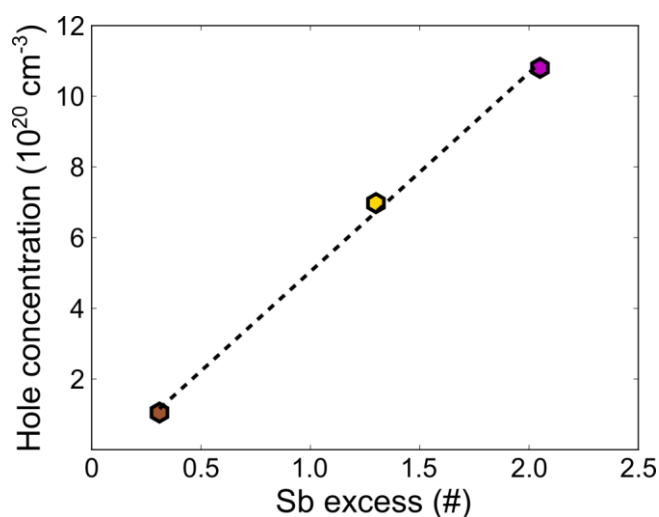
sample.

Figure S5: Room temperature hole concentration (hexagons) as a function of the Sb excess, calculated from the XRD fits, of the $Sb_{2+x}Te_3$ films grown on miscut Si. The linear fit (dashed black) is a guide to the eyes.

The electrical conductivity σ and the power factor $S^2\sigma$ as a function of the Sb excess are

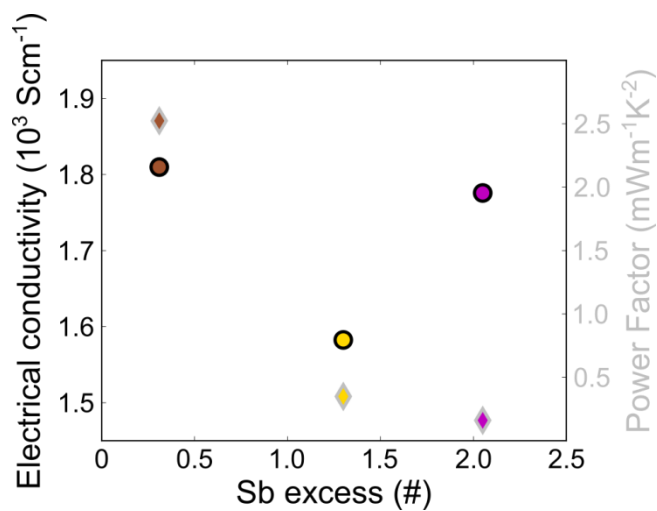shown in Figure S6, circles and diamonds respectively.

Figure S6: Room temperature electrical conductivity (circles with black borders) and power factor (diamonds with gray borders) as a function of the Sb excess of the $Sb_{2+x}Te_3$ films grown on miscut Si.

References

[1]   S. Cecchi, R. N. Wang, E. Zallo, R. Calarco, *Nanosci. Nanotechnol. Lett.* **2017**, *9*, 1114.

[2]   H. Steiner, V. Volobuev, O. Caha, G. Bauer, G. Springholz, V. Holý, *J. Appl. Crystallogr.* **2014**, *47*, 1889.

[3]   K. Sakamoto, K. Miki, T. Sakamoto, H. Yamaguchi, H. Oyanagi, H. Matsuhata, K. Kyoya, *Thin Solid Films* **1992**, *222*, 112.

[4]   C. W. Pei, B. Turk, J. B.   roux, W. I. Wang, J. Héroux, *J. Vac. Sci. ...* **2001**, *19*, 1426.

[5]   T. Kageyama, T. Miyamoto, M. Ohta, T. Matsuura, Y. Matsui, T. Furuhata, F. Koyama, *J. Appl. Phys.* **2004**, *96*, 44.

[6]   E. A. Anyebe, M. K. Rajpalke, T. D. Veal, C. J. Jin, Z. M. Wang, Q. D. Zhuang, *Nano Res.* **2015**, *8*, 1309.

[7]   E. Zallo, S. Cecchi, J. E. Boschker, A. M. Mio, F. Arciprete, S. Privitera, R. Calarco, *Sci. Rep.* **2017**, *7*, 1466.

[8]   Http://www.samx.com/microanalysis/products/stratagem_us.html, STRATAGem.

[9]   S. Cecchi, E. Zallo, J. Momand, R. Wang, B. J. Kooi, M. A. Verheijen, R. Calarco, *APL Mater.* **2017**, *5*, 026107.

[10]   P. F. P. Poudeu, M. G. Kanatzidis, *Chem. Commun.* **2005**, 2672.

[11]   Sb4Te3 Crystal Structure: Datasheet from "PAULING FILE Multinaries Edition – 2012" in SpringerMaterials (https://materials.springer.com/isp/crystallographic/docs/sd_1420181).

[12]   G. C. Sosso, S. Caravati, M. Bernasconi, *J. Phys. Condens. Matter* **2009**, *21*, 095410.

[13]   V. Agafonov, N. Rodier, R. Céolin, R. Bellissent, C. Bergman, J. P. Gaspard, *Acta Crystallogr. Sect. C Cryst. Struct. Commun.* **1991**, *47*, 1141.